Progress Report for the LIBRA Light Ion Beam Fusion Reactor Project for the Period January - June 1983

B. Badger, T. Bartel, J. Billen, M.L. Corradini, R.L. Engelstad, G.L. Kulcinski, E.G. Lovell, G.A. Moses, K.J. O'Brien, R.R. Peterson, L. Pong, M.E. Sawan, I.N. Sviatoslavsky, W.F. Vogelsang, J.J. Watrous

July 1983

FPA-83-3

FUSION POWER ASSOCIATES

2 Professional Drive, Suite 248
Gaithersburg, Maryland 20879
(301) 258-0545

1500 Engineering Drive
Madison, Wisconsin 53706
(608) 263-2308

Progress Report for the LIBRA Light Ion Beam Fusion Reactor Project for the Period January - June 1983

B. Badger, T. Bartel, J. Billen, M.L. Corradini, R.L. Engelstad,
G.L. Kulcinski, E.G. Lovell, G.A. Moses, K.J. O'Brien,
R.R. Peterson, L. Pong, M.E. Sawan, I.N. Sviatoslavsky,
D.K. Sze, W.F. Vogelsang, and J.J. Watrous

July 1983

FPA-83-3

TABLE OF CONTENTS

INTRODUCTION

This is a progress report of work performed between January 1, 1983 and June 30, 1983 by Fusion Power Associates under contract to Kernforschungszentrum Karlsruhe. The purpose of the work is to investigate critical issues related to light ion fusion reactor development in order to set the stage for a complete conceptual design at a later time. This current work includes:

(1) Physical modeling and computer code development to simulate the propagation of light ions in preformed plasma channels.

(2) Kinetic theory modeling of condensation of liquid metals in the presence of non-condensible gases.

(3) Heat transfer calculations of cavity gas flowing through INPORT units.

(4) Mechanical response of INPORT units to the shock wave from the target generated fireball.

Progress in the work on these topics, as well as a few others, is reported in the remainder of this document.

Papers related to LIBRA that have been published or will soon be published are:

1. R.L. Engelstad and E.G. Lovell, "Dynamic Response and Stability of INPORT Tubes in ICF Reactors," 5th Topical Meeting on the Technology of Fusion Energy, Knoxville, TN, April 1983.

2. R.L. Engelstad and E.G. Lovell, "Strength and Fatigue Analysis of Fibrous Silicon Carbide for ICF Reactor Applications," 3rd Topical Meeting on Fusion Reactor Materials, Albuquerque, NM, September 1983.

3. R.L. Engelstad and E.G. Lovell, "Mechanical Analysis of First Wall Tubes for the LIBRA Conceptual Reactor," 10th Symposium on Fusion Technology, Philadelphia, PA, December 1983.

4. R.L. Engelstad and E.G. Lovell, "Modal Analysis of First Wall Tube Banks for Light Ion ICF Reactors," 2nd International Modal Analysis Conference, Orlando, FL, February 1984.

1. LIBRA Overview and Parameters

At this stage the LIBRA reactor study is at a "critical issues" level of activity. By this we mean that limited resources have been devoted to the careful study of a few key problems associated with light ion beam fusion reactor design rather than taking a very broad, shallow look at many different issues. For this reason, the LIBRA conceptual reactor design does not include a great amount of detail in all of the areas typically studied in a full scale conceptual design project. However, in order to add a degree of specificity to the parameters chosen for the various analyses, an initial abbreviated parameter list has been proposed for LIBRA. This is given in Table 1.1. A cut view of the reaction chamber, water shield, and pulsed power machine is shown in Fig. 1.1. The LIBRA reactor is meant to serve as a demonstration reactor, where all technologies for commercialization must be proven but might not yet be fully economical. The most interesting features of the cavity design are the combination of cavity gas and INPORT tubes to effectively transfer the fireball energy from the cavity gas to the $Pb_{83}Li_{17}$ coolant. The tubes serve as the blanket and also protect the first wall from neutron damage. Another notable feature of LIBRA is the use of a water shield between the target chamber and the pulsed power machine. The advantages and disadvantages of the water shield are still being actively discussed.

The reactor has a relatively low repetition rate of 1 Hz. This is very likely to be altered to a larger value once enough cavity gas-INPORT tube heat transfer calculations have been done to verify the heat transfer rate to the tubes.

The critical issues unique to light ion fusion are mostly associated with the cavity environment. A background gas at a pressure of ~ 10-30 torr must

TABLE 1.1

Major LIBRA Parameters

Reactor Type	Demonstration Electricity Production
Cost Goal	Less than 10^9 $
Ion Accelerator Type	Pulsed Power Diode or Multi-Stage
First Wall Protection	HIBALL-like INPORT Units
Ion Propagation Mode	Preformed Channels or Self-Propagation
Target Yield	320-640 MJ
Repetition Rate	0.75-1.5 Hz
Fusion Power	480 MW
Thermal Power	612 MW
Gross Electric Power	245 MW
Net Electric Power	215 MW

Fig. 1.1

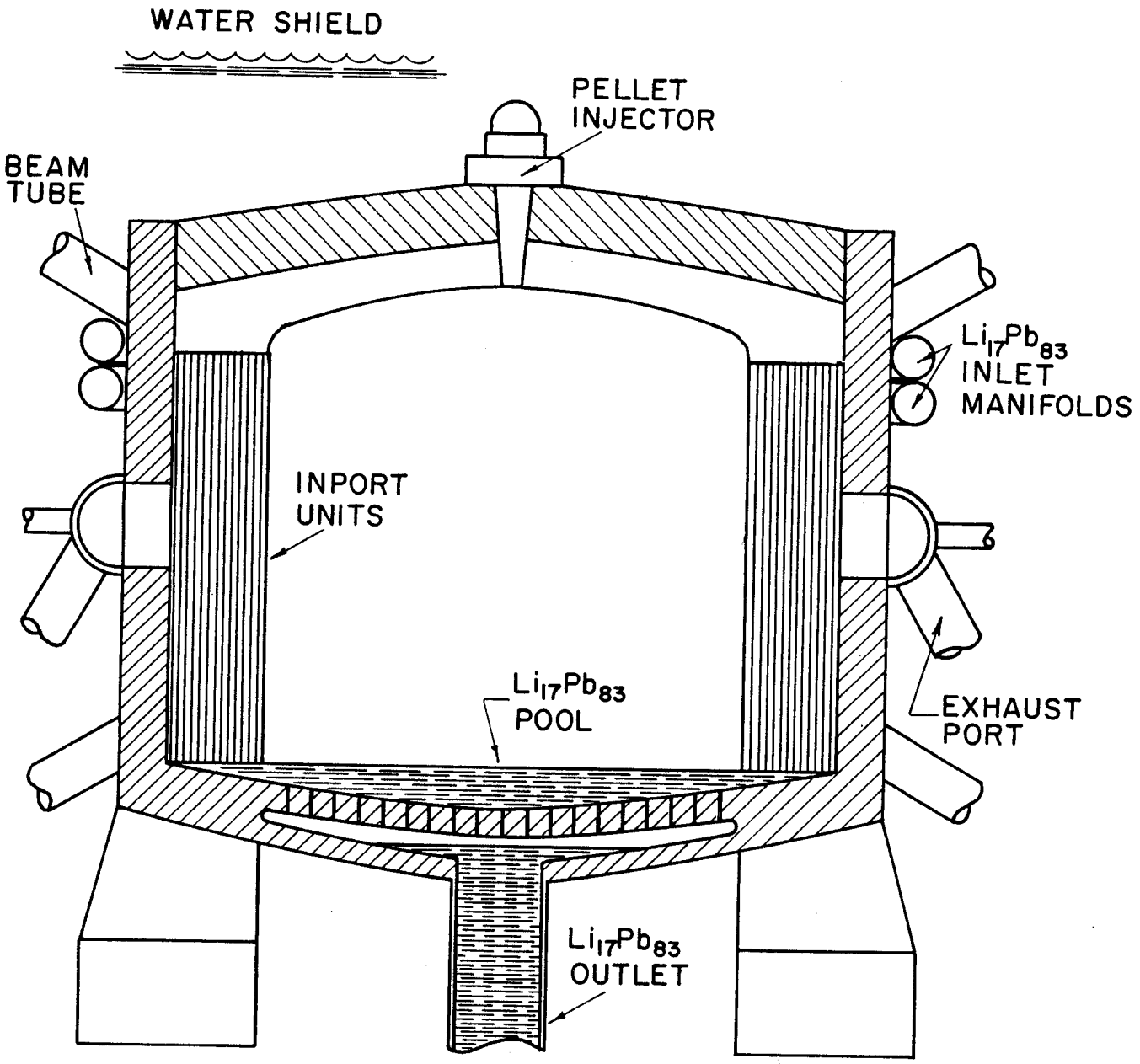

SCHEMATIC OF LIBRA REACTION CHAMBER

be introduced to serve as a medium for preformed z-pinch ion beam transport channels. Computer modeling of channel formation via magneto-hydrodynamic response to a discharge current and the subsequent ion propagation in them are included in this study. After the target explosion, the gas holds up to 30% of the thermonuclear energy. This energy must be effectively transferred from the gas to a working fluid. Models are being developed to compute the energy transferred by the gas to INPORT tubes via radiation and convection. The INPORT tubes will experience the mechanical overpressure resulting from the target fireball. Models are being developed to analyze the mechanical response of flexible tubes held in tension. These three modeling efforts now allow us to turn toward an integrated design of the LIBRA reactor cavity backed up by suitable analysis. More design activity will follow in the second half of this project.

2. Channel MHD Calculations

The dynamics of plasma channel formation will be studied through computer simulations. The main instrument of these simulations will be a modified version of FIRE. The modifications will turn FIRE into a radiation-magneto-hydrodynamic simulator. The progress of the modifications is discussed here.

As it stands, FIRE performs one-dimensional Lagrangian hydrodynamics using a one-fluid, one-temperature model. Included in this model is the coupling between the plasma and the radiation field. The latter is modeled with either multigroup or single group diffusion theory. This results in a set of coupled diffusion equations: one for the plasma temperature, the rest for the radiation. In order to simulate z-pinch channels, FIRE will be expanded to include the effects of electromagnetic fields.

Toward this goal, a new code, MAGDIF, has been written. MAGDIF calculates the magnetic field in an axially and azimuthally symmetric channel. The electric field and Joule heating are also calculated. Like FIRE, MAGDIF has been written following structured programming/structured design principles. The result is a code that may be modified very easily to upgrade the physical models that are used. For example, MAGDIF presently calculates electrical resistivity using the Spitzer model. However, anomalous resistivity is often an important effect. The code's structure is such that the electrical resistivity calculation may be altered without affecting any other portion of the code.

MAGDIF calculates the magnetic field using a magnetic diffusion equation:

$$\frac{1}{c}\frac{\partial \vec{B}}{\partial t} + \vec{\nabla} \times \left(\frac{nc}{4\pi}\right) \vec{\nabla} \times \vec{B} = \vec{\nabla} \times \frac{\vec{u}}{c} \times \vec{B} \ .$$

This equation is a combination of Ampère's Law (neglecting displacement current), Ohm's Law, and Faraday's Law. The calculation of B from this equation requires that the value of B at some outer radius be specified. By appealing to Ampère's Law, one may obtain this boundary condition as

$$B(r_o,t) = \frac{2}{r_o c} I(t)$$

where I(t) is the current enclosed by radius r_o. MAGDIF has the option of using a predefined current or of calculating the current from a circuit equation.

The circuit equation used in MAGDIF comes from considering the channel as being an element of an electric circuit, Fig. 2.1. The circuit consists of an external driving capacitor, an external resistance, and the channel's intrinsic resistance and self-inductance. The external circuit parameters are specified by the user. The channel circuit parameters are calculated via

$$R_c = 1/\left(\ell \sum_{n=1}^{N} \frac{A_n}{\eta_n}\right)$$

ℓ = channel length

A_n = cross-sectional area of nth zone

η_n = electrical resistivity of nth zone.

$$L_c = \frac{2U}{I}$$

$$U = \frac{1}{8\pi} \int_{\text{channel}} B^2 \, d^3r \qquad \text{(total magnetic energy in channel)}$$

Fig. 2.1

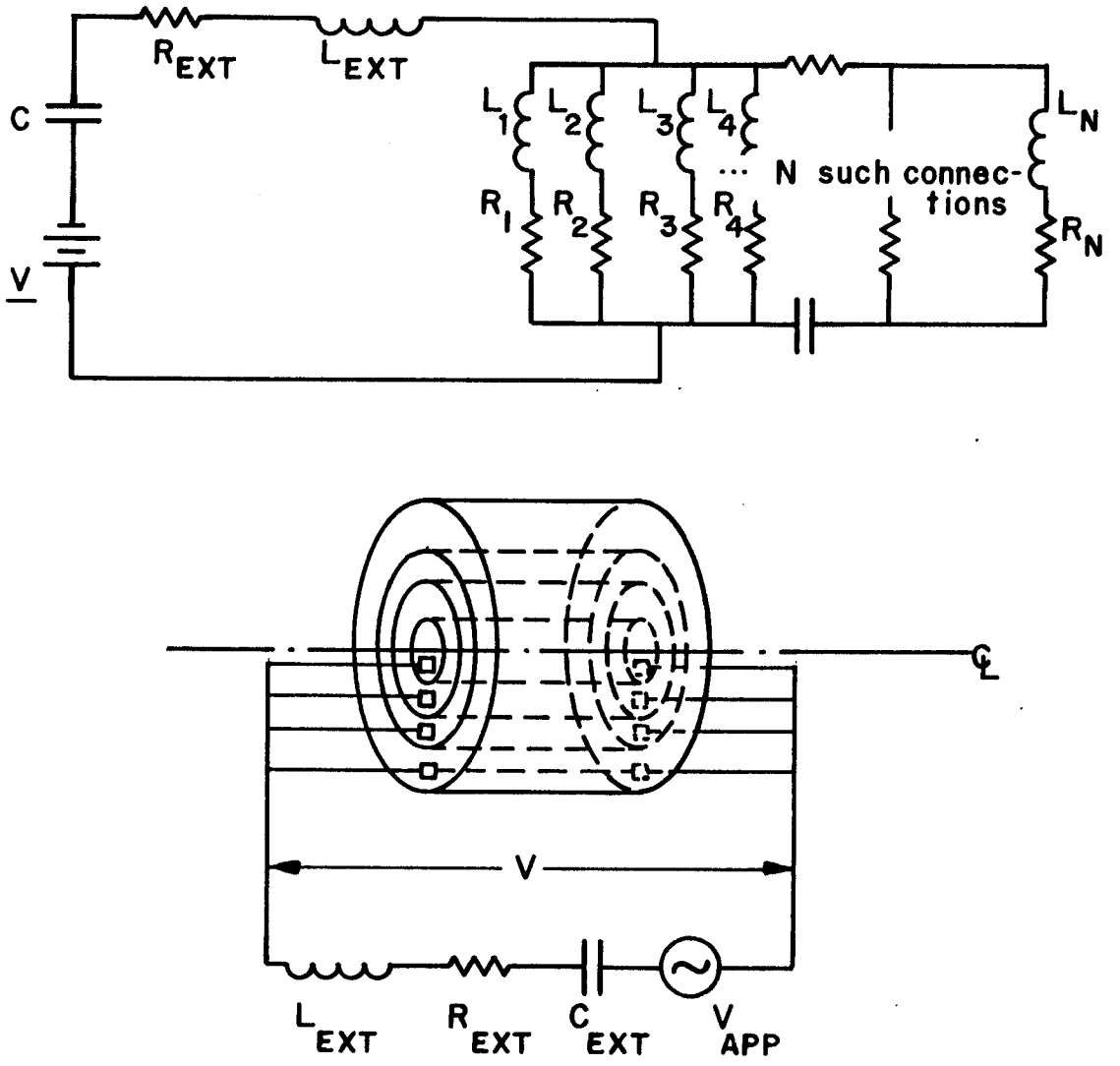
R EXT
L EXT
C
V
L1
L2
L3
L4
... N such connec-
tions
LN
R1
R2
R3
R4
RN
V
L EXT
R EXT
C EXT
V APP

By using Kirchhoff's Laws on the circuit, an equation for the current is obtained:

$$\ddot{I} + \left(\frac{\dot{L}_c + R_{ext} + R_c}{L_c}\right) \dot{I} + \left(\frac{\dot{R}_c + 1/C_{ext}}{L_c}\right) I = 0 \ .$$

This is a second order, nonlinear ODE. MAGDIF solves this equation using a fourth order Runge-Kutta algorithm (Runge's 4th order method). Since this algorithm requires that values for certain coefficients be specified at future time-steps, a parabolic extrapolation method is used to obtain the channel's resistance and inductance.

The cycle of calculations is pictured below. Once the magnetic field profile has been obtained, the electric field is obtained by integrating Faraday's Law. Fluid-field coupling terms, like Joule heating, may then be calculated.

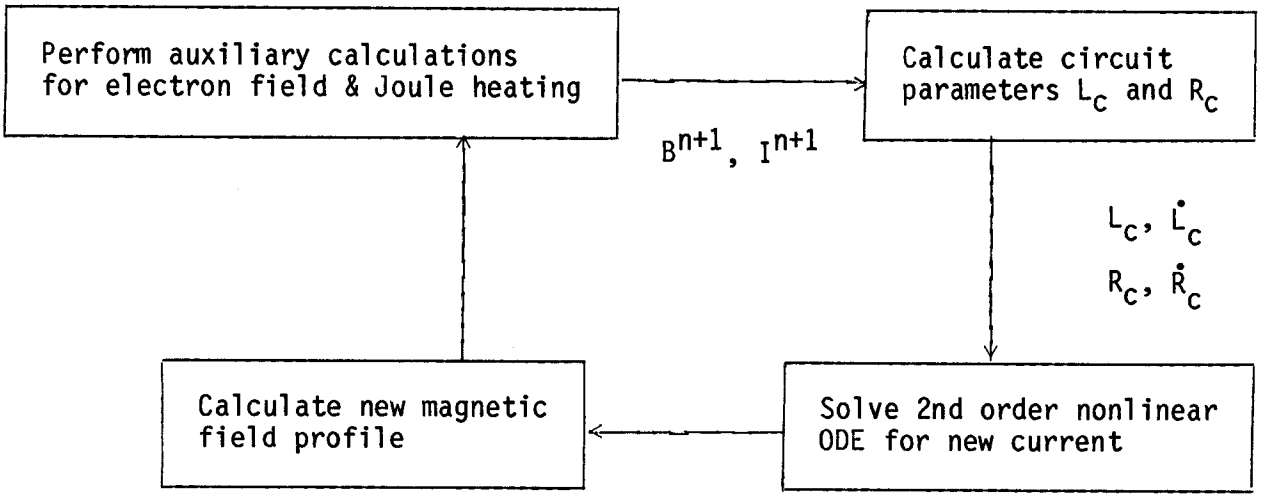

MAGDIF has been tested for the case where there is no fluid velocity and the current is steady. The magnetic diffusion equation for this situation becomes

$$\frac{\partial B}{\partial t} - D \frac{\partial}{\partial r} \frac{1}{r} \frac{\partial}{\partial r} rB = 0 ,$$

boundary data $\begin{cases} B(r=0,t) = 0 , \\ B(r=r_o,t>0) = (2/r_o c)\, I \end{cases}$

initial condition $\{B(r,t=0) = 0.$

An analytic solution to this problem has been obtained:

$$B(r,t) = \frac{2I}{r_o^2 c} \left\{ r - 2r_o \sum_{n=1}^{\infty} \frac{J_1\left(\nu_n \frac{r}{r_o}\right)}{\nu_n J_2(\nu_n)} e^{-(D\nu_n^2/r_o^2)t} \right\} .$$

A comparison between this solution and MAGDIF's solution is shown in Figs. 2.2 and 2.3.

When MAGDIF has been fully debugged and tested, it will be coupled into FIRE. There are a number of tests that remain to be performed. One is to test the code's solution for the case that the current is governed by the current equation rather than being steady. Analytic work in this area is now beginning. Another test will be to compare different finite difference schemes for the solution of the magnetic diffusion equation. At present, MAGDIF uses a numerical scheme very similar to that developed by Ray Kidder for his MAGPIE code. Comparisons between this scheme and more standard schemes, such as that used in FIRE for the temperature diffusion equation, are now being undertaken.

Fig. 2.2

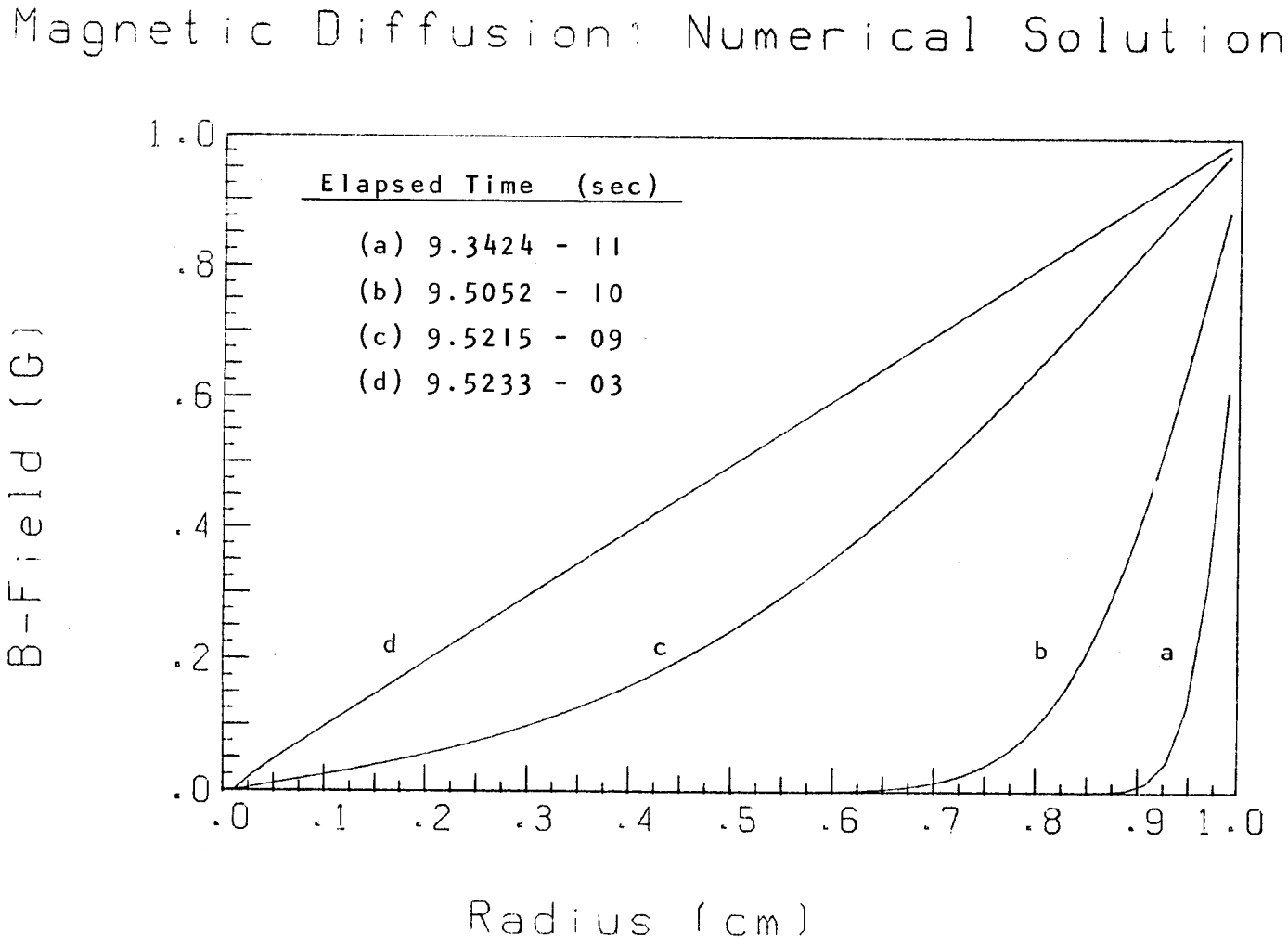
Magnetic Diffusion: Numerical Solution
Elapsed Time (sec)
(a) 9.3424 - 11
(b) 9.5052 - 10
(c) 9.5215 - 09
(d) 9.5233 - 03
B-Field (G)
Radius (cm)
1.0
.8
.6
.4
.2
.0
.0 .1 .2 .3 .4 .5 .6 .7 .8 .9 1.0
a
b
c
d

Fig. 2.3

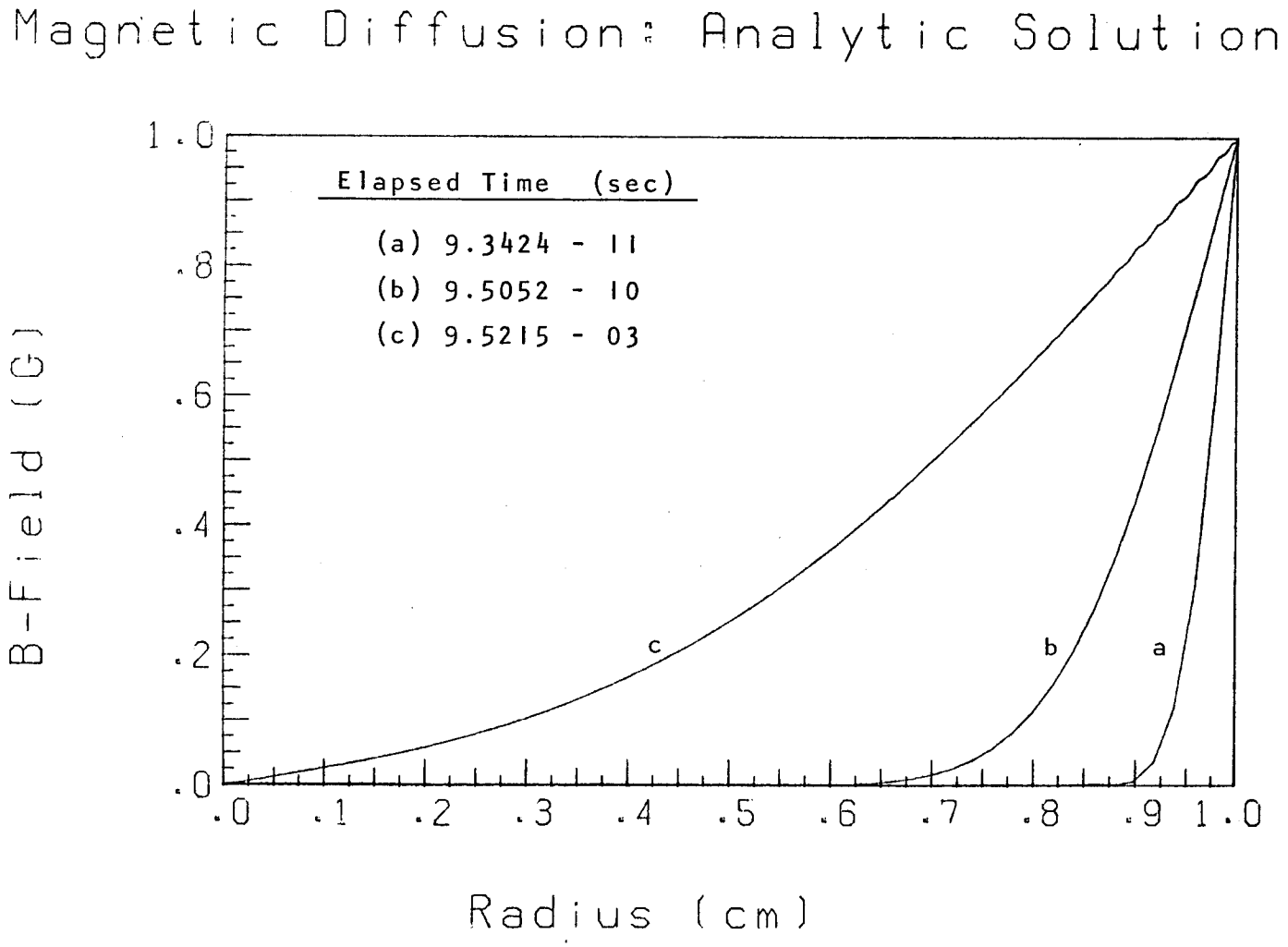
Magnetic Diffusion: Analytic Solution
Elapsed Time (sec)
(a) 9.3424 - 11
(b) 9.5052 - 10
(c) 9.5215 - 03
B-Field (G)
1.0
.8
.6
.4
.2
.0
.0 .1 .2 .3 .4 .5 .6 .7 .8 .9 1.0
Radius (cm)
a
b
c

In addition to the tests mentioned above, future work includes an investigation of more sophisticated physical models. Anomalous resistivity appears to be a very important effect in experiments. A generalized Ohm's Law, and its incorporation into MAGDIF will also be investigated.

3. Ion Beam Propagation

The problem of modeling intense light ion beam propagation in the LIBRA reactor is being approached in three phases. The first phase was to model the z-pinch plasma channel as a perfectly space and current neutralizing medium and to calculate the ion trajectories in the azimuthal magnetic field created by externally driving a current in the channel. Examples of these simple calculations were presented in the last LIBRA progress report. This trajectory model of Ottinger, Goldstein and Mosher has been further extended to include the effects of nonperfect space and current neutralization through the inclusion of two factors, f_e and f_m, such that the net fields within the ion beam are given by

$$E_r(r) \approx 2\pi q n_0 r(1 - f_e)$$

$$B_\theta(r) \approx 2\pi q n_0 \beta r(1 - f_m) \ .$$

Starting from the equations of motion of the ions the following equation for radial motion of a beam ion is obtained,

$$\ddot{r} + \alpha r - e\dot{r} = \delta r^{-3} + \sum_{n=2}^{N} B_n r^n$$

where dots refer to derivatives with respect to the axial coordinate z, and the following definitions have been made,

$$\varepsilon = - \frac{\beta\dot{\beta}}{\beta_0 c}$$

$$\alpha = \frac{qB_1}{\beta_o mc^2} - \frac{2\pi q^2 n_o}{\beta_o mc^2}\left[1 - f_e - \beta_o^2(1 - f_m)\right]$$

$$\delta = \left(\frac{P_\theta}{m\beta_o c}\right)^2$$

$$\beta\dot{\beta} = (\beta\dot{\beta})_{\text{collision}} + (\beta\dot{\beta})_{\text{axial field}} .$$

The last term in the trajectory equation refers to a simple model for the magnetic field that takes account of different profiles. Ions near the leading edge see a magnetic field quite different than ions at the trailing edge where the fields have been swept outward by the heated and expanding plasma.

Leading edge ions see:

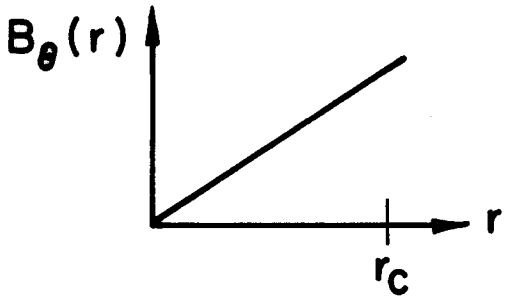

Trailing edge ions see:

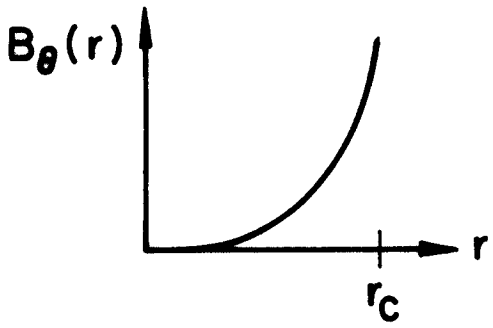

Applying a simple Liapunov stability analysis to the radial equation, which describes a nonlinear autonomous oscillator, in the case of a leading edge ion, one finds the equilibrium points

$$(\dot{r},r) = \left(\frac{\delta}{2}\right)^{1/4} (\pm 1,0)$$

corresponding to the system,

$$\dot{r} = \dot{x}_1 = x_2$$

$$\ddot{r} = \dot{x}_2 = -\alpha x_1 + \varepsilon x_2 + \delta x_1^{-3} .$$

Linearizing the system about this point and computing the eigenvalues results in:

$$\lambda = \frac{1}{2}\,\varepsilon \pm \sqrt{\varepsilon^2 - 4\alpha} .$$

The angular momentum has no effect upon the stability of the orbit, except to influence the position of the nodes, as one realizes by noting that δ has dropped out of the eigenvalues.

The key to applying this simple extension of the orbit analysis is to compute f_e and f_m. To do this we must model the response of the background plasma to the passage of the ion beam. This has been done by solving the equations

$$\frac{4\pi}{\omega_p^2}\frac{\partial \vec{J}}{\partial t} + \frac{1}{\sigma}\vec{J} = \vec{E}$$

$$\vec{J}_b(r,u) = q_b v_n f(u) n(r) \tilde{v}$$

$$n_b(r,u) = q_b f(u) n(r)$$

where $u = z - v_b t$ is the wavefront variable. To these we add Maxwell's equations

$$\nabla \times \vec{B} - \frac{1}{c}\frac{\partial \vec{E}}{\partial t} = \frac{4\pi}{c}\vec{J}$$

$$\nabla \times \vec{E} + \frac{1}{c}\frac{\partial \vec{B}}{\partial t} = 0$$

$$\nabla \cdot \vec{B} = 0$$

and maintain charge neutrality by using

$$\left(\frac{\partial \rho}{\partial t} + \nabla \cdot \vec{J}\right)_b = \left(\frac{\partial \rho}{\partial t} + \rho \cdot \vec{J}\right)_\rho = 0$$

in place of Poisson's equation. These equations are solved using Fourier transform techniques that will not be reproduced here in detail.

Examples of the calculations that have been done to date are given in the following figures. In Fig. 3.1 we show the ion beam charge distribution, Gaussian along the z axis and a Bennet profile in the radial direction. Plots of the radial and axial electric field components and the azimuthal magnetic field component are shown in Figs. 3.2 to 3.4. In these figures the beam envelope extends in the radial direction from $r = 0$ to $r = 1$ and the channel boundary is at $r = 2$. The conductivity of the channel ($r < 2$) is small but finite and the conductivity outside of the channel is zero. The axial and radial electric fields serve to pull electrons into the beam to neutralize it and to expel electrons once the beam has passed. These plasma response calcu-

Fig. 3.1

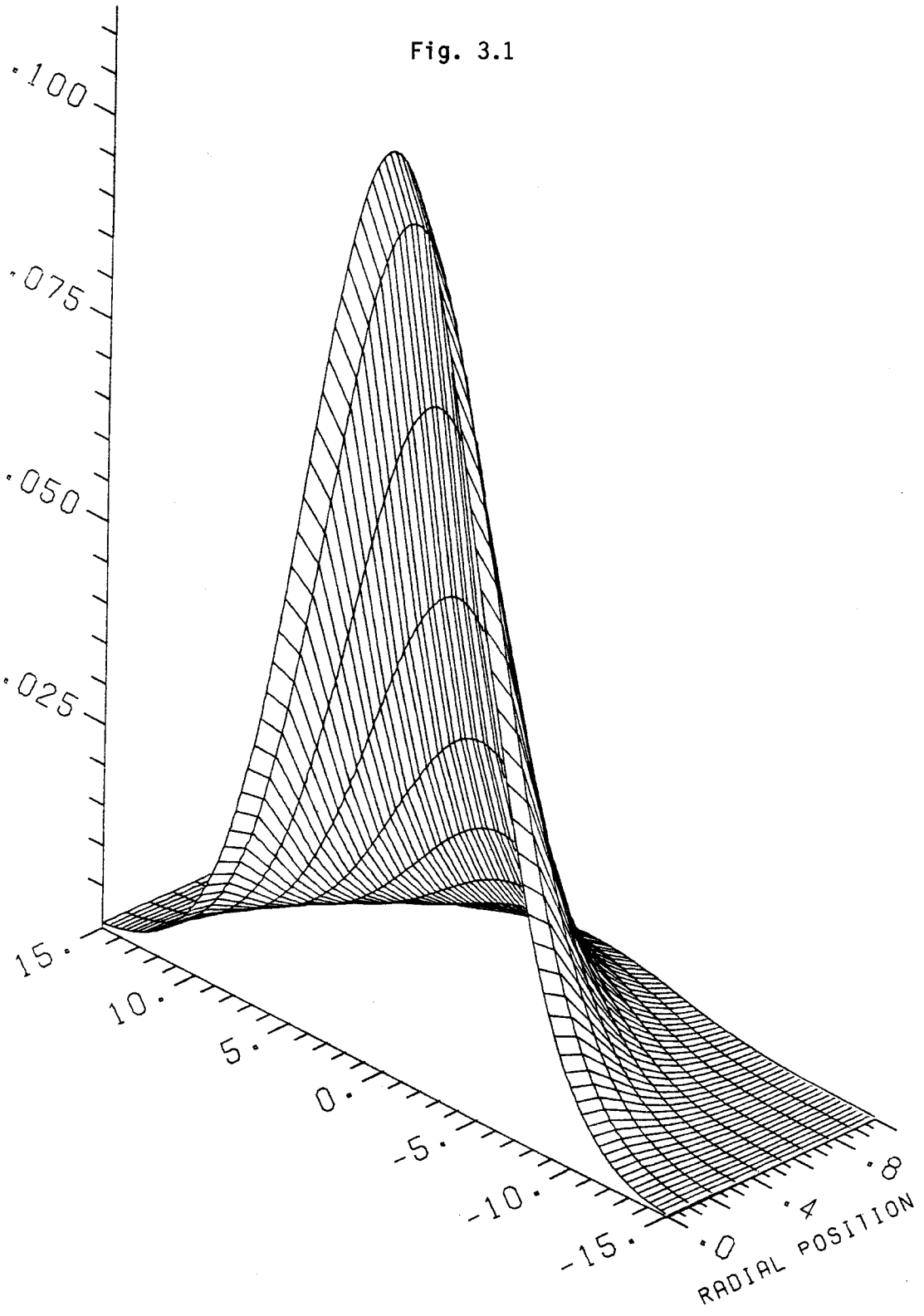

ION BEAM CHARGE DENSITY

Fig. 3.2

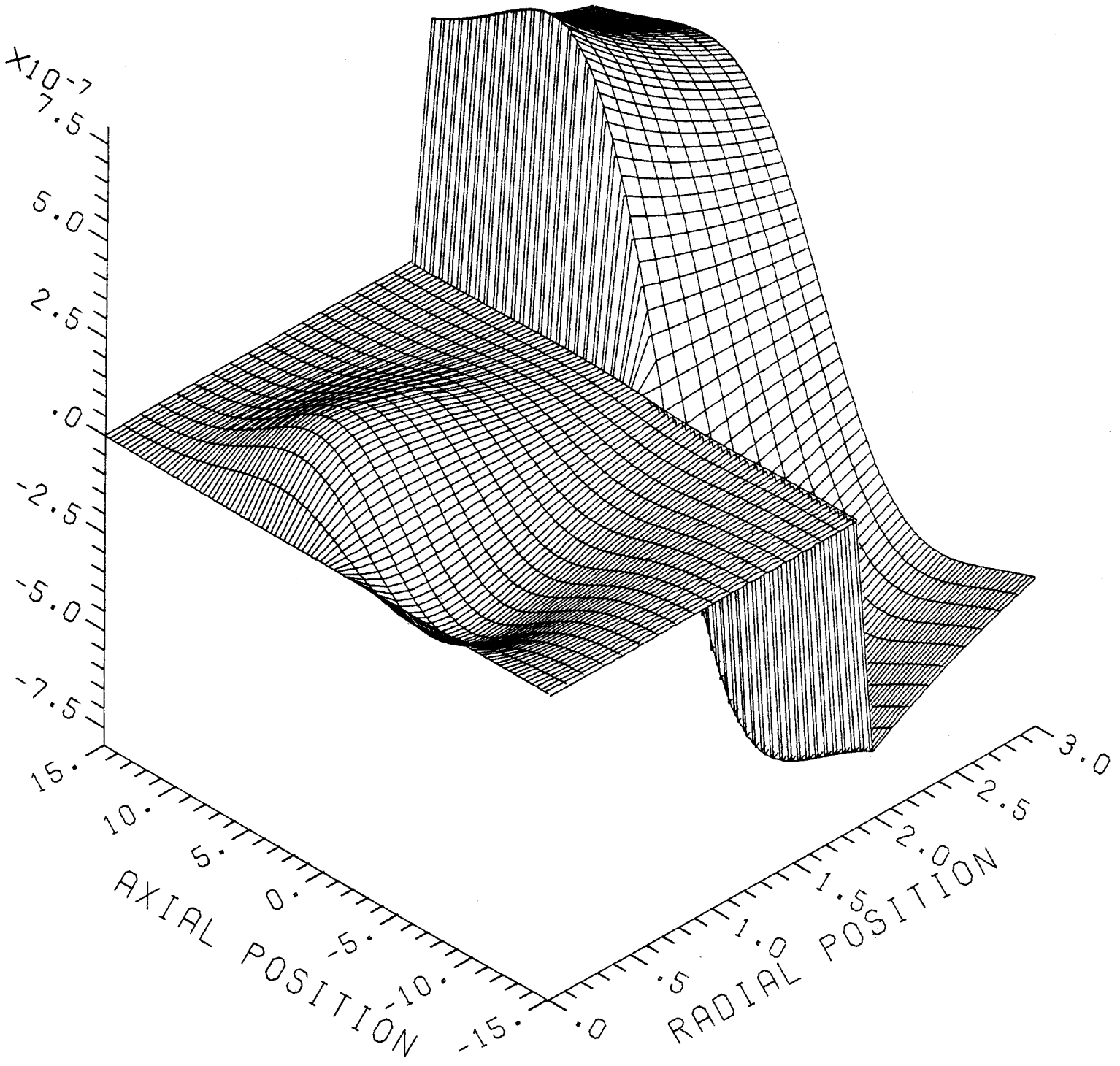

RADIAL ELECTRIC FIELD

Fig. 3.3

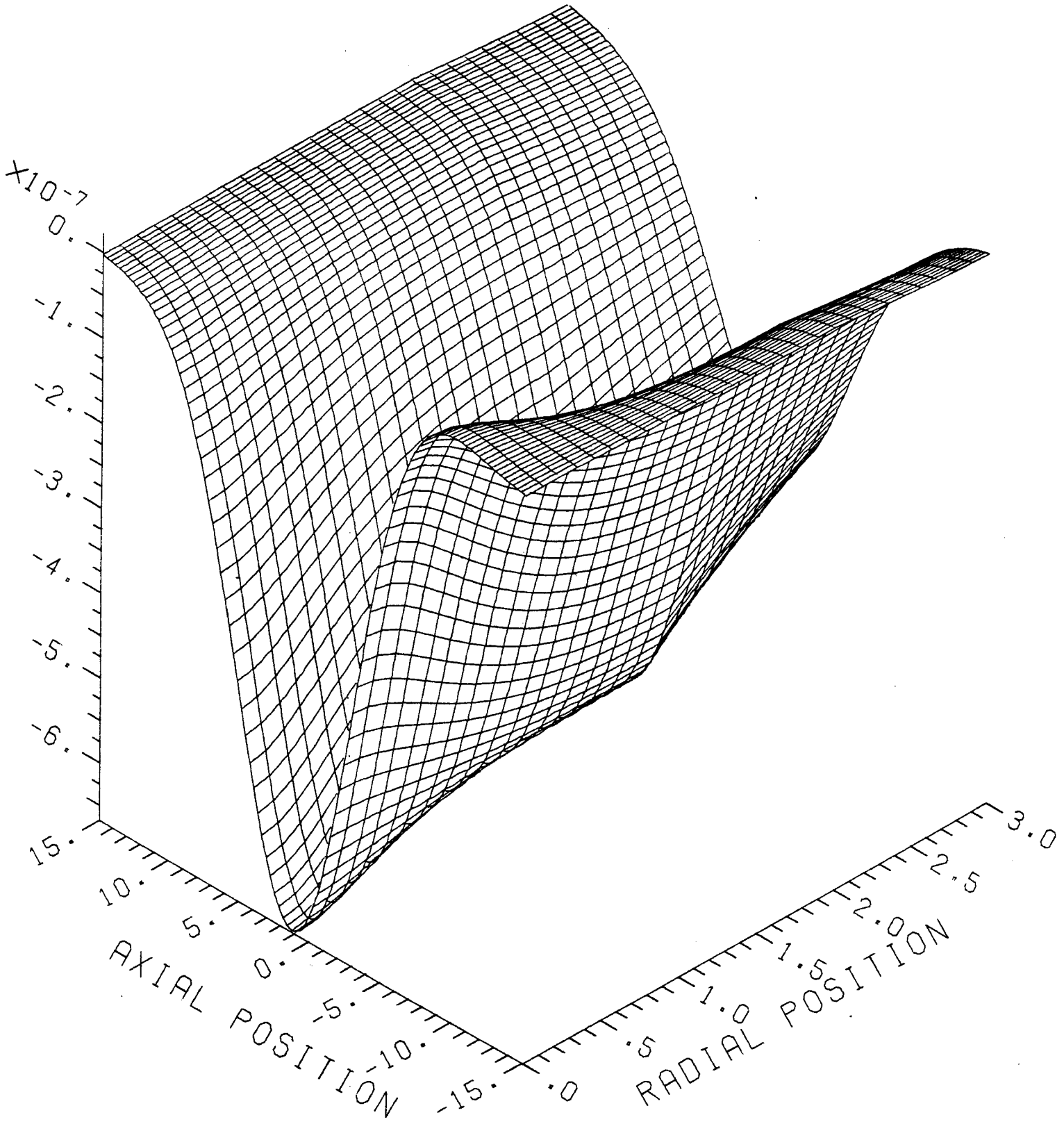

AXIAL ELECTRIC FIELD

Fig. 3.4

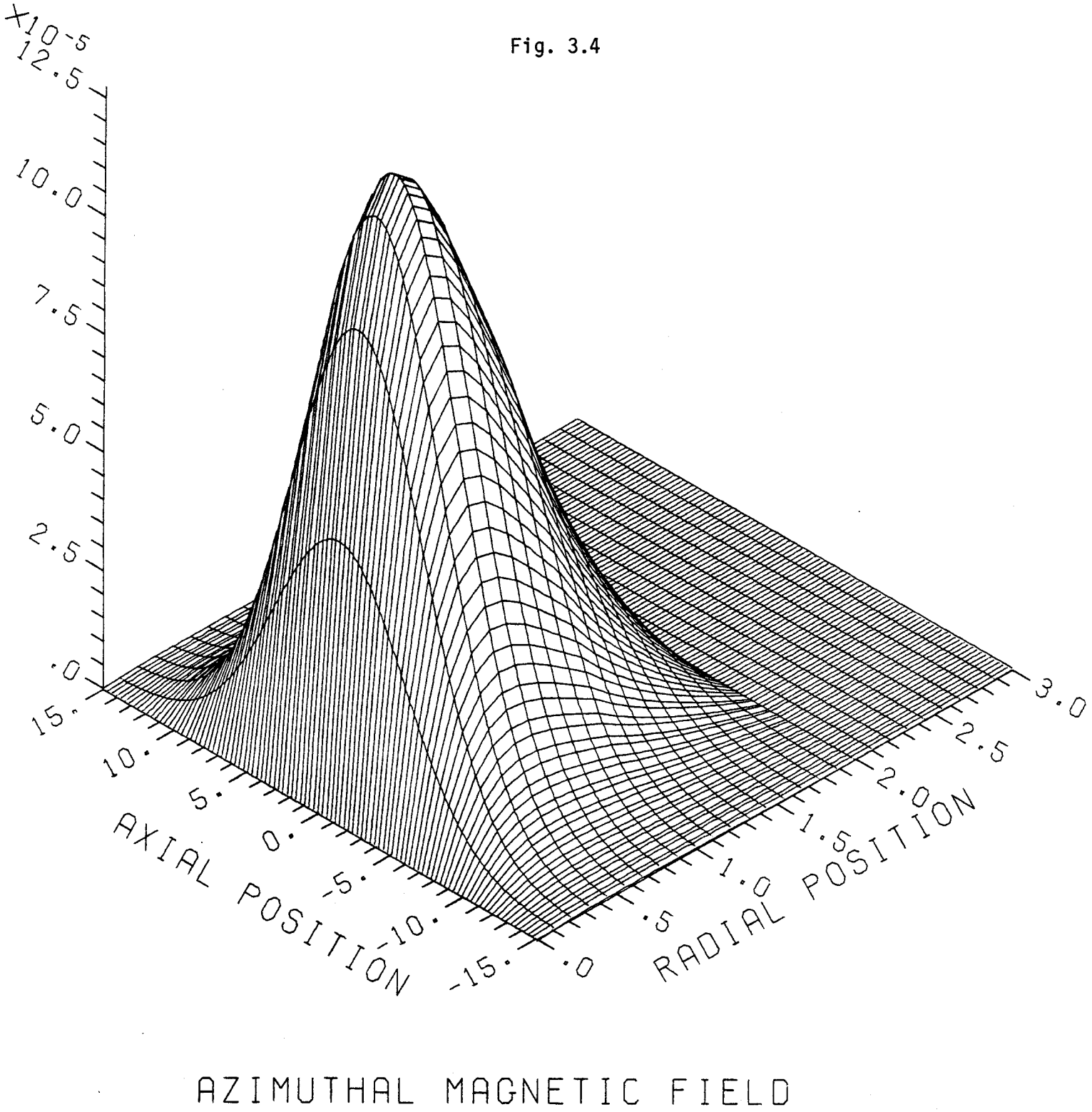

AZIMUTHAL MAGNETIC FIELD

lations will allow us to calculate f_e and f_m. These calculations represent the second phase of our modeling.

The third phase of modeling will be to attempt a kinetic treatment of the beam-plasma channel system. Work has not yet begun on this problem.

4. Liquid Metal Condensation

The problem of liquid metal condensation is critical to any reactor design where the first wall is protected by liquid metals, such as HIBALL and LIBRA. We have continued work that was first reported in the last HIBALL Annual Report (1982), Fusion Power Associates Report FPA-82-6, Chapter 2.3. We model a system of condensible and non-condensible gas using a modified form of the kinetic theory treatment of Labuntsov and Kryukov.[1] They treated the problem of only a condensible gas as shown in Fig. 4.1 using a combination of fluid equations in the gas dynamic region I and a kinetic theory treatment in the so-called Knudsen layer. They used the Grad 13-moment distribution function for a single species. We have advanced this approach to include two gas species, condensible and non-condensible gas, and consequently use the form of the Grad 13-moment distribution function for two species

$$f_i = n_i \left(\frac{m_i}{2\pi kT}\right)^{3/2} e^{-\zeta_i^2} \left[1 + \frac{1}{2}\frac{P_{i1}}{P_{ik}}\left(3\,\zeta_{ix}^2 - \zeta_i^2\right) + \frac{2\,q_i\zeta_{ix}\left(\frac{2}{5}\zeta_i^2 - 1\right)}{P_{ik}(2R_iT)^{1/2}} + \left(\frac{7}{2} - \zeta_i^2\right)\zeta_{ix}\left(\frac{2}{R_iT}\right)^{1/2} V_{di}\right] \qquad i = 1,2$$

1 = condensible gas

2 = non-condensible gas

to describe the distribution of each species in the Knudsen layer. In the gas dynamic region we assume that the two species have Maxwellian distributions. Formulating the mass, momentum and energy equations in regions I and II (see Fig. 4.1) and matching them at the K-K interface and applying appropriate boundary conditions we obtain 17 nonlinear algebraic equations in 17 unknowns.

Fig. 4.1

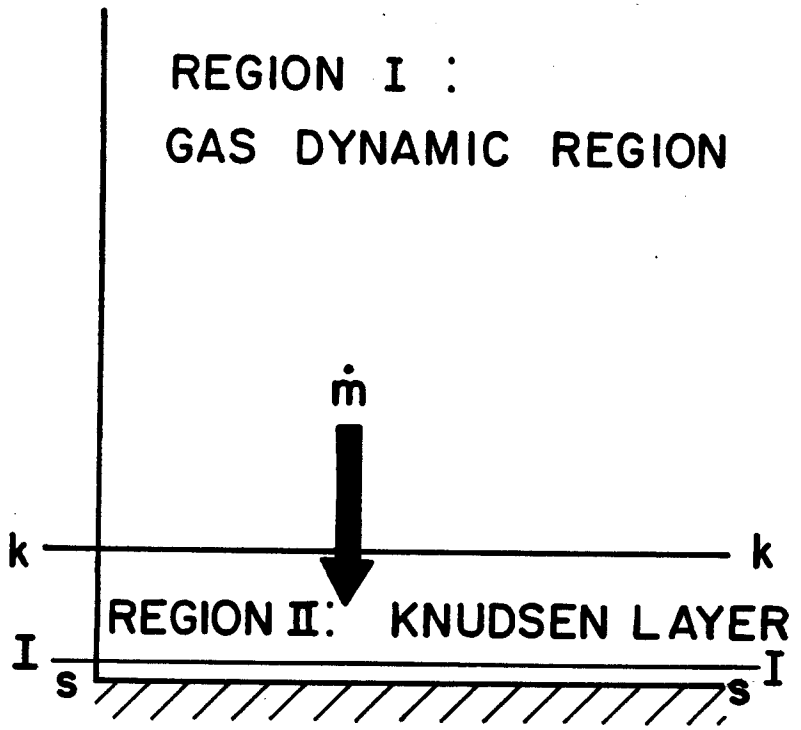
REGION I :
GAS DYNAMIC REGION
ṁ
k
k
REGION II: KNUDSEN LAYER
I
I
s
s

These equations will not be included here due to their complexity. In the future, a report will be released with details of this analysis.

These nonlinear equations are solved numerically using a combination of algorithms designed to minimize the sum of squares.[2] Our first results are plotted in Fig. 4.2. In this figure the condensation rate is normalized to the rate that one would obtain for no non-condensible gas present. The normalized condensation rate is plotted as a function of the ratio of non-condensible to condensible gas for different atomic masses of non-condensible gas. The condensible gas is assumed to be lead. We can see that the condensation rate is a steep function of this density ratio and asymptotically approaches the diffusion limit as the ratio becomes large. We have verified that in the limit of no non-condensible gas, we obtain the same absolute condensation rate as Labuntsov and Kryukov.

We believe that the initial steep drop in condensation rate is due to Knudsen layer effects while the more gradual behavior for larger gas density ratios is due to collisional resistance from the bulk fluid. Knudsen layer effects are due to a buildup of the non-condensible gas density at the condensing surface as shown schematically in Fig. 4.3. This is due to the decrease in condensible gas density at the surface and the constraint that the total pressure of the system be equal everywhere. The Knudsen layer effect at small density ratios is the most interesting aspect of this work and we will continue by concentrating on a range of parameters with $n_{\text{non-condensible}}/n_{\text{condensible}} \approx 1$.

Fig. 4.2

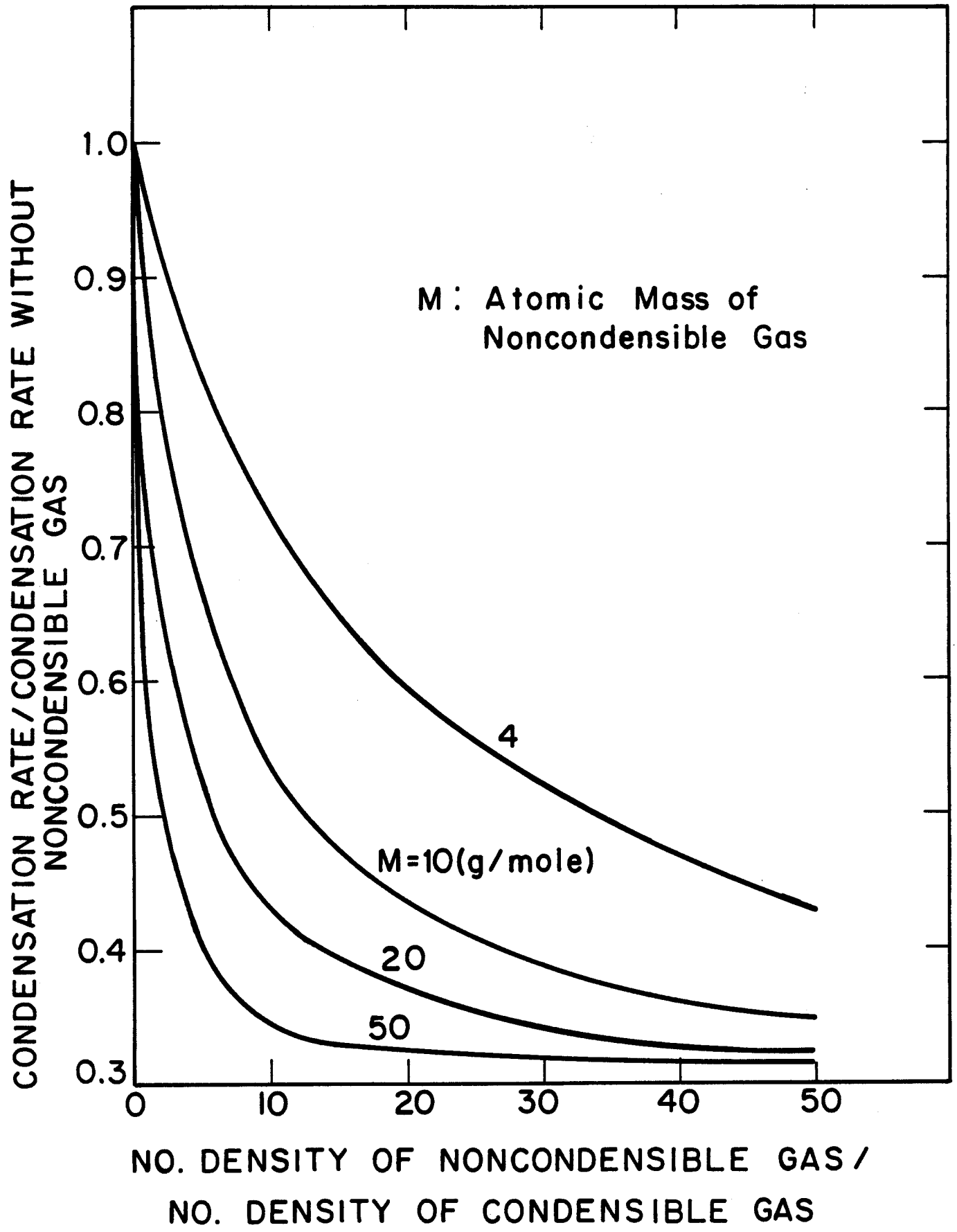
CONDENSATION RATE/CONDENSATION RATE WITHOUT NONCONDENSIBLE GAS
1.0
0.9
0.8
0.7
0.6
0.5
0.4
0.3
0
10
20
30
40
50
M: Atomic Mass of Noncondensible Gas
4
M=10(g/mole)
20
50
NO. DENSITY OF NONCONDENSIBLE GAS / NO. DENSITY OF CONDENSIBLE GAS

Fig. 4.3

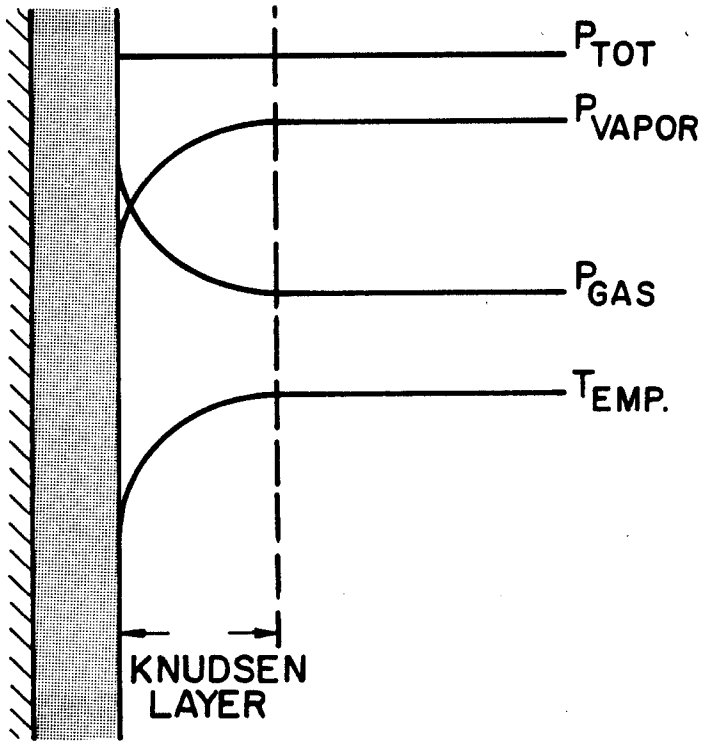

THE PRESSURE AND TEMPERATURE DISTRIBUTION FOR VAPOR-GAS MIXTURE

References for Section 4

1. D.A. Labuntsov and A.P. Kryukov, "Analysis of Intensive Evaporation and Condensation," Int. J. Heat Mass Transfer 22, 989 (1979).

2. Nonlinear Optimization Routines - User Manual for the 1100, University of Wisconsin Computing Center Report.

5. Mechanical Response of INPORT Units

In this section, the cavity first wall system is described and results are presented for the response of the system to repetitive loading.

The cylindrical cavity of LIBRA is encircled by an annular tube bank of INPORT units - tubular components with pliable porous walls of silicon carbide fiber. As shown in Fig. 5.1, $Li_{17}Pb_{83}$ flows axially within the INPORTs and also through the tube walls to develop a thin protective outer film. INPORTs can be braided as seamless tubes with sufficient axial fiber to provide extensional stiffness or alternatively an orthogonal weave fabric could be used to produce a tube with inherently better axial strength and stiffness but having the disadvantage of a seam. For such applications, SiC yarns are typically composed of 500 filaments, each approximately 10 μ in diameter. Filaments are homogeneously composed of ultrafine β-SiC crystals with excess carbon, manufactured by polymer pyrolosis.

It is proposed that INPORTs be supported at both the top and bottom of the LIBRA cavity. The schematic design of Fig. 5.2 would permit assembly from the top and pretension by means of compression spring systems. Flanged ends of INPORTS can be rigidized and strengthened for support by chemical vapor deposition of additional SiC.

The primary loading on LIBRA INPORTs is the dynamic overpressure which propagates through the cavity gas. A pulse of this type determined from the FIRE code is shown in Fig. 5.3. For current calculation purposes it is assumed that the shock transmission to the tube is based upon a rigid surface model; a less conservative estimate would result if surface movement was assessed. Vibration frequencies of INPORTs have been calculated and from Fig. 5.4 it can be seen that tension variations have a modest influence on fre-

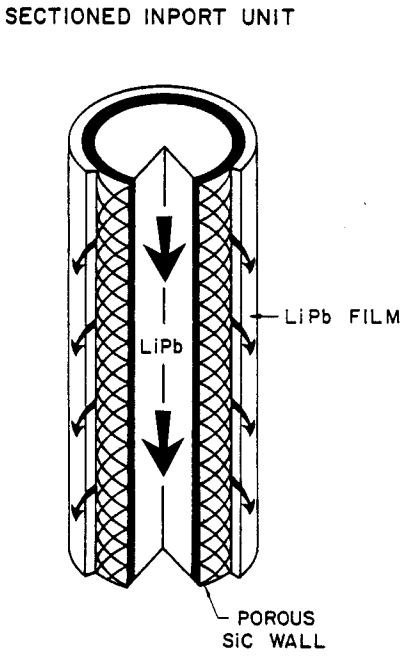

Fig. 5.1

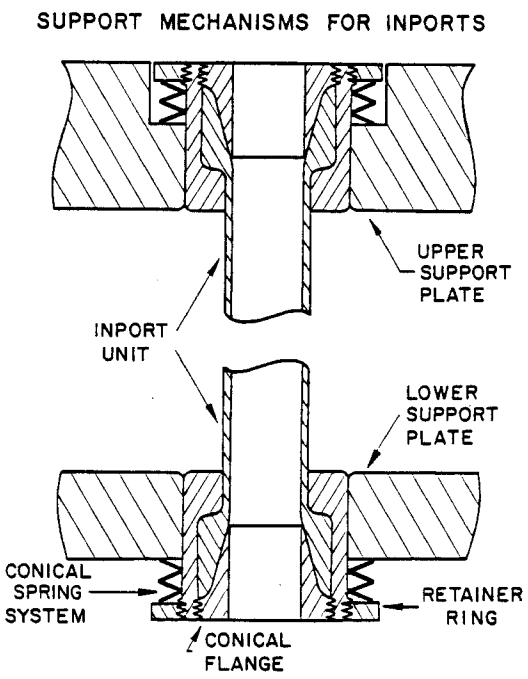

Fig. 5.2

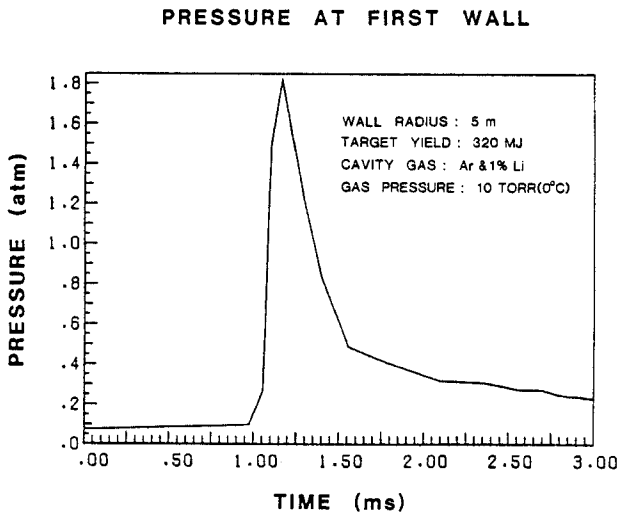

Fig. 5.3

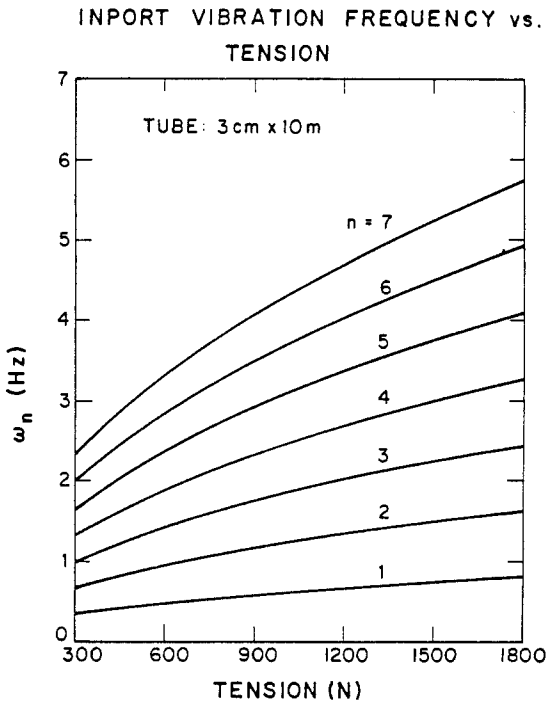

Fig. 5.4

quencies for lower modes and a stronger effect on higher modes. For a nearly uniform dynamic pressure, the largest contribution to the total motion will be from the fundamental mode, the natural frequency of which is less than 1 Hz (Fig. 5.4). Since the repetition rate of the LIBRA cavity is expected to be greater than 1 Hz, resonance effects should not be a problem. In addition, the vibration period of INPORTs is so much larger than the pulse width of the shock that its influence will be practically the same as an impulse.

A computer code has been developed for the determination of the response of INPORTs to dynamic sequential pressure pulses for tubes of various lengths, levels of damping and pretensions. Calculations presented are based upon the loading of Fig. 5.3 (impulse of 87 N sec/m^2) and a tube diameter of 3 cm. From Fig. 5.5 it can be seen that modest increases in tension substantially reduce displacements but larger increases are not relatively as effective. A decrease in length substantially reduces the midpoint displacement as shown in Fig. 5.6. In contrast, the results of Fig. 5.7 indicate that changes in the damping level do not produce dramatic changes in response, particularly for steady state amplitude. This is also shown in Fig. 5.8 which includes the academic case of 99% critical damping. Maximum transient displacement and steady state amplitude are plotted in Figs. 5.9 and 5.10 for different tensions and damping. The steady state curve for 20% damping should be a practical guide for the determination of the radial spacing of the INPORTs. Finally Fig. 5.11 shows a typical transient and steady state response for sequential impulses applied for 3 seconds followed by shutdown. The free vibration of INPORTs following load cessation does not appear to have unusual characteristics requiring special design considerations.

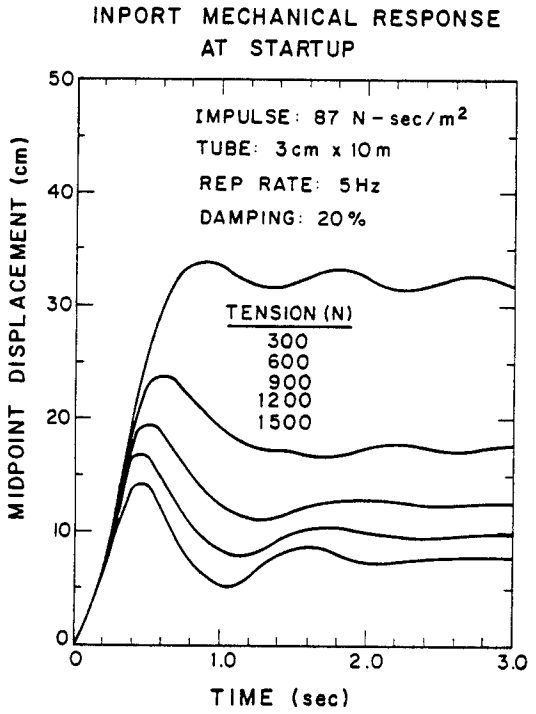

Fig. 5.5

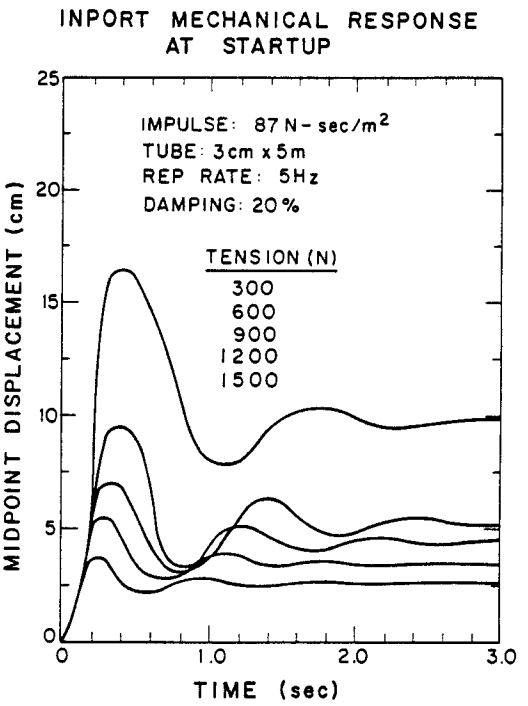

Fig. 5.6

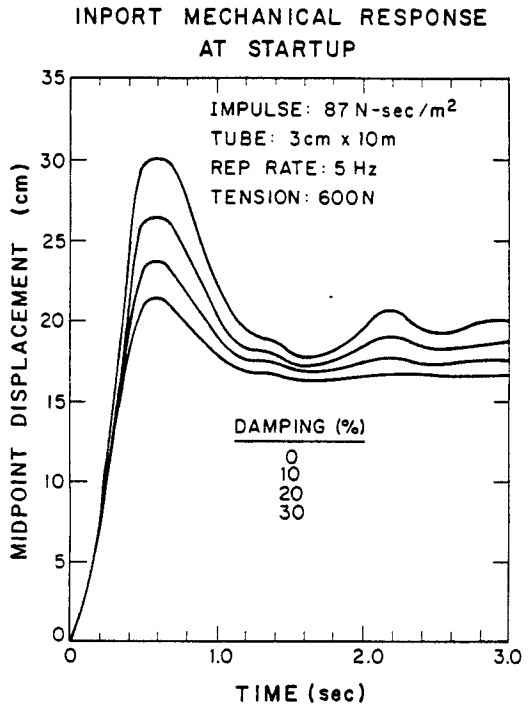

Fig. 5.7

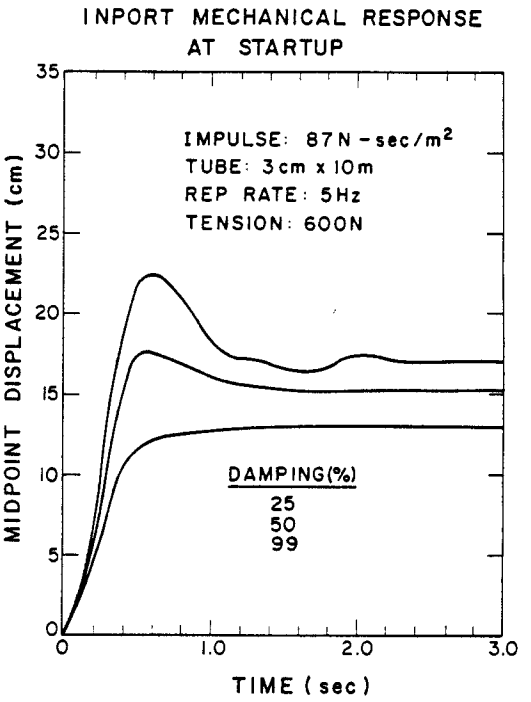

Fig. 5.8

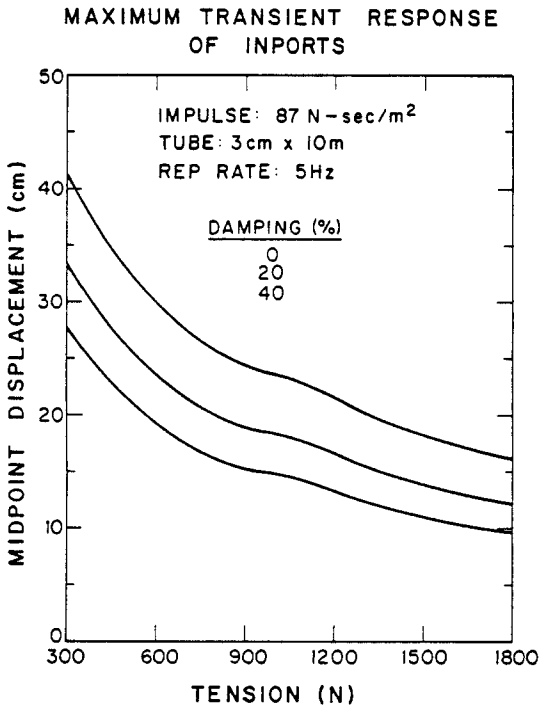

Fig. 5.9

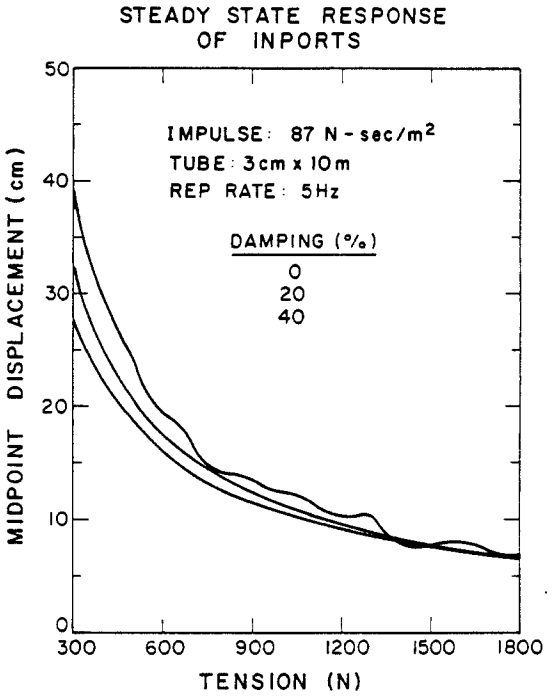

Fig. 5.10

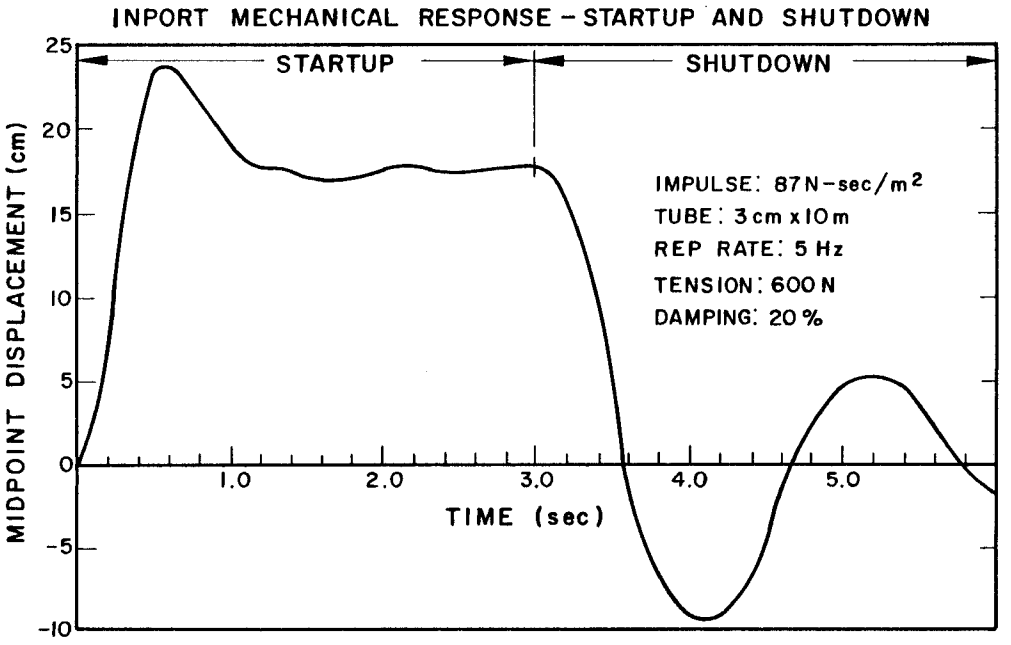

Fig. 5.11

6. INPORT Tube Gas Dynamics and Heat Transfer

6.1 Introduction

The purpose of this investigation is to characterize the heat transfer from the expanding weakly ionized plasma through the INPORT tube region of the LIBRA reactor cavity. This phase of the cycle occurs as the gas begins to propagate around the tubes (1.5 msec after the event) after undergoing a free expansion in the center of the cavity. Although the temperature of the gas is much lower (3000°K) than the extremely high plasma temperature of the "fireball," approximately 8.4% of the design energy release (320 MJ) remains as sensible heat and kinetic energy. Therefore, this energy removal process must be sufficiently understood so that the gas temperature can be reduced to a value determined by ion transport requirements within the design cycle time and without excessive heat flux loading on the tube surface.

A detailed characterization of the gas-tube heat transfer process is extremely difficult due to the geometry, initial conditions, and wall boundary conditions. Figure 6.1 illustrates the complicated gas cross-flow geometry at the cavity midplane. The inner two rows of tubes are of smaller diameter (3 cm) than the remainder (10 cm) due to heat flux considerations during the intensive thermal radiation flux from the "fireball." The initial fluid conditions are such that vortex shedding (von Kàrmàn) could be expected to occur. Second, all the tubes have porous walls and a liquid metal film is expected to exist on their exterior throughout the entire cycle. The interaction of high speed flow over a bluff body with a surface film has not been extensively investigated. Finally, the gas pulse is supersonic (M_∞ = 2.5) when it enters the INPORT tube region. It is expected that bow shocks will form on the first row as well as reflected shocks from the curved surfaces.

Fig. 6.1

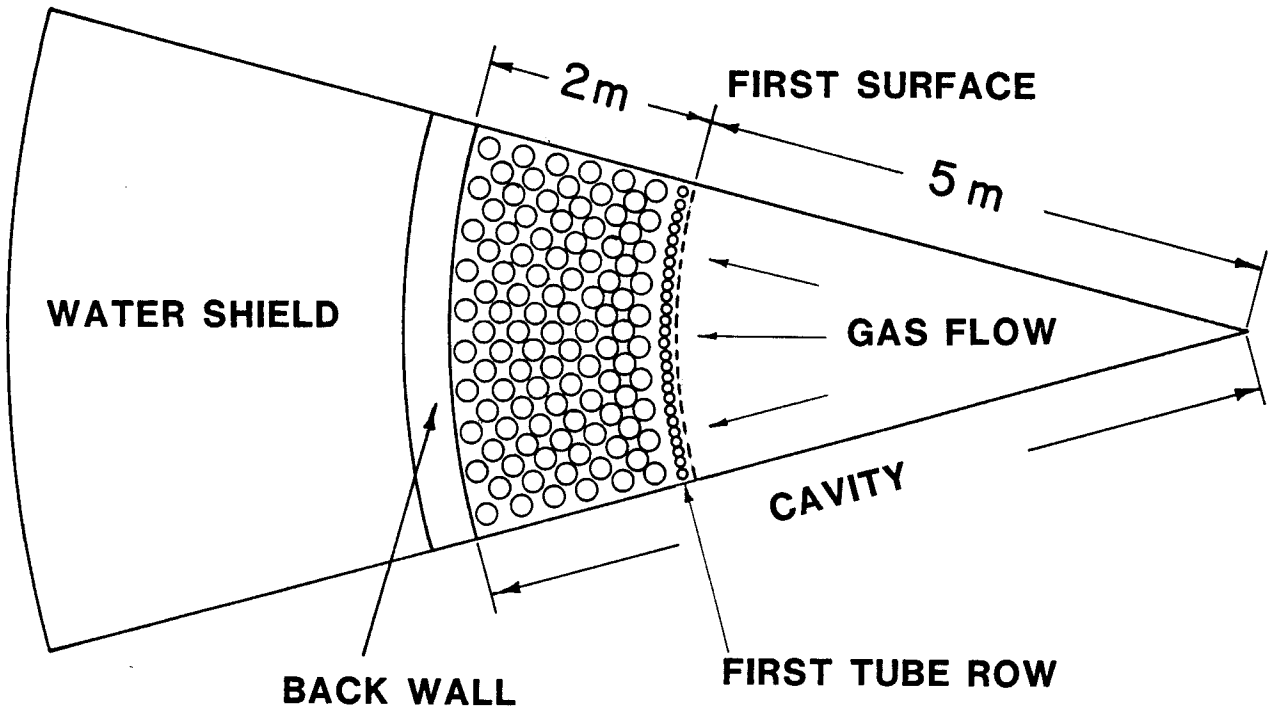
2m
FIRST SURFACE
5 m
WATER SHIELD
GAS FLOW
CAVITY
BACK WALL
FIRST TUBE ROW

In short, the following modeling assumptions and phenomenological mechanisms are important to adequately characterize the heat transfer process: viscous compressible flow, radiation heat transfer, convective heat transfer, film entrainment and vaporization, skin friction, form drag, and condensation. Of these, only condensation will probably not be important due to the process time constants.

6.2 Initial Gas Conditions

The initial conditions for the gas pulse incident on the first row of INPORT tubes are given in Table 6.1. The pressure, velocity and density data were obtained from a FIRE calculation. The pulse is being modeled as a square wave in the present investigation. There are a few quantities to take particular note of in the table. The first is the pulse pressure; it is very low. This will present modeling difficulties due to the high total drag experienced at the first row of tubes (i.e., choking the supersonic flow). It is this quantity which mandates the use of a viscous-compressible model (along with the freestream Mach number). Next, the initial energy of the pulse is partitioned such that 18% is in the sensible heat of the gas and 82% in the kinetic energy. Thus, gas temperatures much higher than the inlet 3000°K are to be expected in the tube bank as momentum transfer thermalizes the pulse. And finally, the pulse width is approximately 100 cm (the INPORT tube region is 200 cm). A crude Lagrangian computer model indicated that the pulse would rapidly become much longer at the first tube row (> 200 cm). Therefore, the current computer model solves the steady state continuum equations on an Eulerian mesh. Knudsen number calculations based on the gas mean free path and a characteristic length of either the tube diameter or bow shock stand-off

Table 6.1

Temperature	3000°K
Pressure	2.23 N/cm^2
Density	3.6×10^{-5} g/cm^3
M_∞	2.5
Velocity	2.5×10^5 cm/s
Re_d	2.12×10^4
Pulse Width	100 cm

distance support the use of the continuum Navier-Stokes equations in lieu of a rarefied gas formulation.

6.3 Survey Calculations

Many survey calculations have been performed with various levels of complexity in an effort to determine the critical phenomena of the process. Two will be briefly discussed here.

The first is a bounding calculation to determine an upper estimate on the time required for the gas temperature to cool to 800°K. It was a homogeneous lumped parameter model for thermal radiation from the gas stagnation temperature (about 9000°K) to the wall temperature. A surface emissivity of 0.15 and a global view factor of 0.80 were assumed. The result was it required 26 msec for the initial gas (9.2 kg) to cool to 800°K with only radiation heat transfer. Convective heat transfer and vaporization were not included. This very small time is due mainly to the large heat transfer surface area of the tubes.

The second calculation was to determine the stagnation heat flux on the first tube row. This is the highest surface heat flux on the surface. Two contributions were calculated: a convective component due to the viscous boundary layer and radiation heat transfer from the stagnation temperature at the edge of the boundary layer to the wall. The results are a heat load of 1.1 kW/cm^2 for convection and 6.3 kW/cm^2 for radiation for a total heat load of 7.4 kW/cm^2. The tubes experience a much higher heat load during the initial phase of radiation heat flux from the fireball (a peak value of approximately 140 kW/cm^2).

6.4 Gas Dynamic Model

A computer model to predict the gas temperature as the pulse propagates through the tube bank is still under development. As discussed earlier, the

geometry and boundaries do not lend themselves to a detailed multi-dimensional Navier-Stokes finite difference approach. Rather, a control volume approach with appropriate correlations to model important mechanisms has been chosen. The main assumptions and features of the model are briefly:

1) Radial Eulerian Control Volumes (1 for small tubes, 10 for others)
2) Continuum Fluid Mechanics
3) Viscous Compressible Fluid Equations (with choking)
4) Supersonic & Subsonic Drag Correlations
5) Local Tube Averaged Convective Heat Transfer Correlations
6) Variable Transport Properties.

Only preliminary results are available using inviscid and near-inviscid fluid and are for code checkout purposes only (energy has been successfully conserved). Currently, a full viscous fluid with choking conditions is being studied.

6.5 Future Work

The present investigation will continue to identify the mechanisms which govern the heat transfer process and attempt to model them. In certain areas, for example entrainment from bluff bodies, the available literature is very limited. Further analysis will be performed to determine the importance of these issues. With this level of modeling and our previously developed models one can then attempt to design the "forest" of INPORT tubes to be consistent with: (i) gas-tube heat transfer, (ii) radiation damage to the first wall, (iii) blanket energy recovery and tritium breeding, (iv) mechanical response of the INPORT tubes, and (v) the INPORT tube lifetime.

7. Gas Handling Systems Outside the LIBRA Reaction Chamber

Since it is not clear yet whether argon or helium gas will be used in the reaction chamber, we have started to look at schemes for handling the gas circulated for impurity control. We therefore postulate that the reaction power is taken out entirely by the LiPb in the tubes. Thus only the fraction needed to maintain a reasonable partial pressure of DT in the cavity (and He in the case of argon) is circulated through a purification system. This quantity has been earlier determined to be 10^{-3} of the chamber volume per shot which is equal to 0.315 moles/sec (STP) for a 5 m radius chamber, 10 m high.

The two enclosed figures (Figs. 7.1 and 7.2) show possible schemes for handling the gases outside the reaction chamber.

7.1 Argon Case

In the argon case, the gas is exhausted from the chamber at 800 K and 30 torr and goes through a series of coolings and compressions emerging at 300 K and 75 torr. Roots pumps are used very effectively in this pressure range and the 0.315 moles/sec requires a pump power of ~ 20 kW. The gas then goes to an oxidizer and then to a molecular sieve, where the water D_2O, T_2O and DTO is recovered. In order to remove the He ash, the argon gas must be liquified. This is done with a LN_2 refrigerator which requires ~ 100 kW of power at room temperature. The pure argon gas can now be reinjected into the reaction chamber.

The water collected in the molecular sieve is put through electrolysis, the O_2 removed and the hydrogen species are condensed, balanced and then used in pellets.

Figure 7.1

ARGON GAS HANDLING SYSTEM

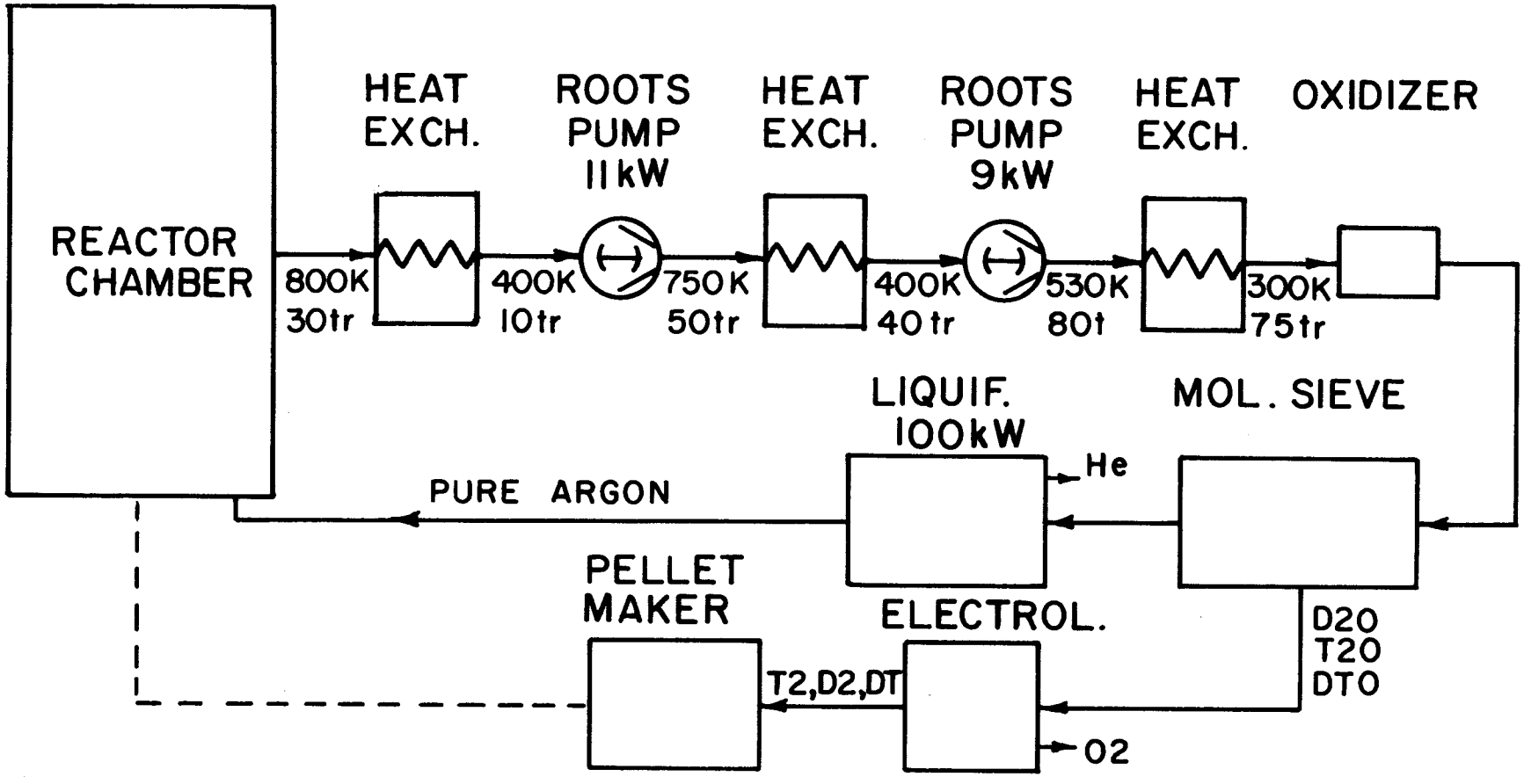

ASSUMED MASS RATE
0.315 MOLES/S.(STP)

Figure 7.2

HELIUM GAS HANDLING SYSTEM

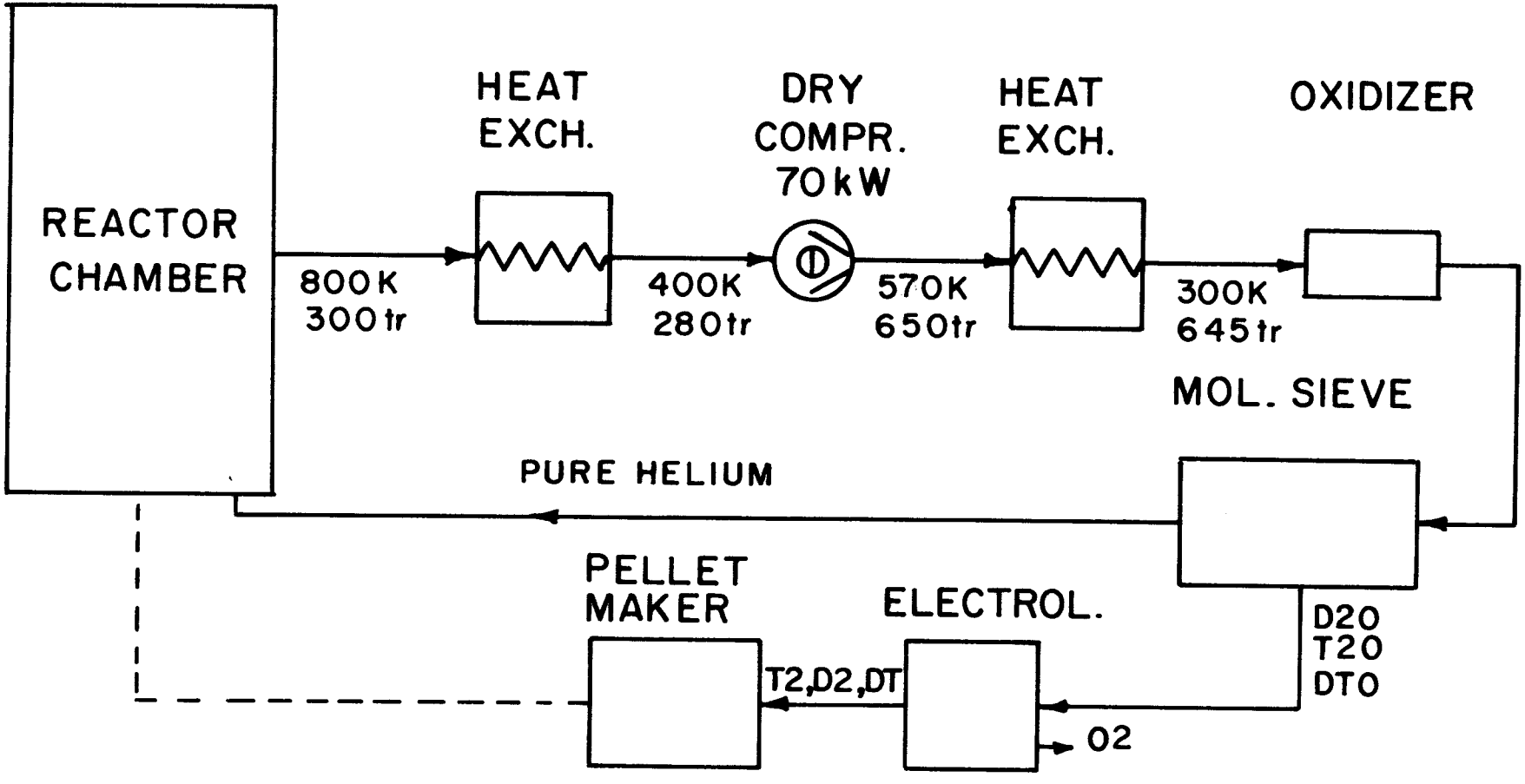

ASSUMED MASS RATE
0.315 MOLES/S.(STP)

7.2 Helium Case

Since helium has less stopping power than argon, it will have to be exhausted at 800 K and 300 torr (100 torr at 300 K). Roots pumps cannot be used at this pressure, therefore dry compressors are proposed which do not contaminate the effluent with oil. Only one stage of compression is needed and two stages of cooling, with the gas emerging at 300 K and ~ 650 torr.

As in the case of argon, the hydrogen species are oxidized, collected on molecular sieves, and then go through electrolysis. After the molecular sieve the helium is pure and can be reinjected into the reaction chamber. The pumping power is estimated at ~ 70 kW.

Yet to be determined is the power needed in the electrolysis process and the exact size of the heat exchangers.